IEEE Robotics and Automation Letters (RA-L) paper, presented at ICRA 2023, London, UK. Cite as RA-L paper.

Modeling the locomotion of articulated soft robots in granular medium

Yayun Du, Jacqueline Lam, Karunesh Sachanandani, and M. Khalid Jawed

***Abstract*—We introduce a numerical tool for modeling articulated soft robots that couples discrete differential geometry-based simulation of elastic rods, our model for the articulated structure, and other external forces. Parallel to simulations, we build an untethered robot testbed, in the granular medium, comprised of multiple flexible flagella that are rotated about an axis by a motor. Drag from the granules causes the flagella to deform and the deformed shape generates a net forward propulsion. External drag depends on the flagellar shape, while the change in flagellar shape is the result of the competition between the external loading and elastic forces. We find reasonable quantitative agreement between experiments and simulations. Owing to a rod-based kinematic representation of the robot, the simulation can run faster than real-time in some cases, and, therefore, we can use it as a design tool for this class of soft robots. We find that there is an optimal rotational speed at which maximum efficiency is achieved. Moreover, both experiments and simulations show that increasing the number of flagella from two to three decreases the speed of the robot. This indicates that our simulator is potentially applicable for unknown physics exploration. We also gain insight into the mechanics of granular medium - while resistive force theory can successfully describe the propulsion at low number of flagella, it fails when more flagella are added to the robot.**

***Index Terms*—Soft robotics, biomimetics, locomotion, design and modeling, bacteria, flagella, discrete elastic rod, granular medium, resistive force theory.**

I. Introduction

SOFT robots and continuum robots inspired by nature that mimic echinoderms, bacteria, and fish, are primarily composed of intrinsically soft matter and fluids, enabling them to deform elastically into reversible shapes [1]–[3]. Their modeling and control are particularly challenging due to the geometric nonlinearity induced by the structural flexibility and the nontrivial coupling among elasticity, contact, and other external forces such as hydrodynamic and magnetic forces.

Compared with well studied underwater locomotion [4], [6], the mechanisms behind underground locomotion are far less understood. Slender flexible animals have evolved to apply various locomotion modes depending on their physiology and environmental factors [7]–[9]. Unlike the Navier-Stokes equations for fluids, no validated theories for locomotions on or inside terrestrial surfaces exist until recently, when the granular flow is shown to be functionally equivalent to low Reynolds fluid [10]. Flagellar propulsion, widely studied since 1955 [11] for application in low Reynolds fluids, is effective in granular media (GM) as well [12]. This builds a remarkable connection between the microscopic world of bacteria [13] and meter-sized snakes in sand. Moreover, the design and control of soft robots usually require painstaking trials due to the limitations of current simulators. Previous work on soft robot modeling has focused on the Finite Element Method [14], voxel-based discretization [15], and modeling of slender soft appendages with Cosserat rod theory [6] (including the piecewise constant strain method [33], piecewise variable strain method, differential kinematics [34], the constant curvature model, and piecewise constant curvature model [35]). A real-time simulator that can conveniently incorporate geometry and external forces will accelerate robot design and explore unknown physics in a complicated environment. Moreover, a simple-to-deploy testbed can greatly benefit theoretical and computational verification.

In this paper, we draw inspiration from the bacterial locomotion and introduce a palm-sized untethered robot comprised of $n \geq 2$ naturally straight elastic rods and a rigid head with an embedded motor and battery. As shown in Fig. 1, the rotation of these *tails* generates drag from the GM, deforming the soft material. The tails provide a net propulsive force as a result of their nonlinear deformation. This net propulsion is only feasible in flexible structures; propulsion is zero in the case of *rigid* straight tails. We introduce a numerical method for simulating the dynamics of a collection of Kirchhoff elastic rods [17] subjected to viscous drag described by Resistive Force Theory (RFT) [11]. This computational tool is used to simulate the multi-limbed robot and quantitatively compared against experiments. We conduct parametric studies on the speed of the robot as a function of the number of tails and rotational speed, and determine the optimal rotational speed for maximum efficiency. We test the applicability of RFT to GM and indicate regimes in which it can fail.

This paper is organized as follows. Section II introduces the background and related work. Section III provides a detailed description of the robotic platform and the experimental setup. Next, the numerical model we employ for simulating the locomotion of multi-limbed robot is introduced in Section IV. The results from simulations and experiments are presented in Section V. Finally, conclusions are summarized and future research directions are suggested in Section VI.

II. Background and related work

Simulating the dynamics of soft robots is complex and slow because of the numerous degrees of freedom and nonlinear material properties. Modeling soft robot locomotion can be

Manuscript received: December 2, 2021; Revised: February 25, 2022; Accepted: April 16, 2022. This paper was recommended for publication by Editor Cecilia Laschi upon evaluation of the Associate Editor and Reviewers' comments. This work was supported by the Henry Samueli School of Engineering and Applied Science, University of California and the National Science Foundation (Award numbers: IIS-1925360, CMMI-2053971, CAREER-2047663). The authors are with the Department of Mechanical & Aerospace Engineering, University of California Los Angeles, Los Angeles, California 90095 USA. Digital Object Identifier (DOI): see top of this page.

IEEE Robotics and Automation Letters (RA-L) paper, presented at ICRA 2023, London, UK. Cite as RA-L paper.

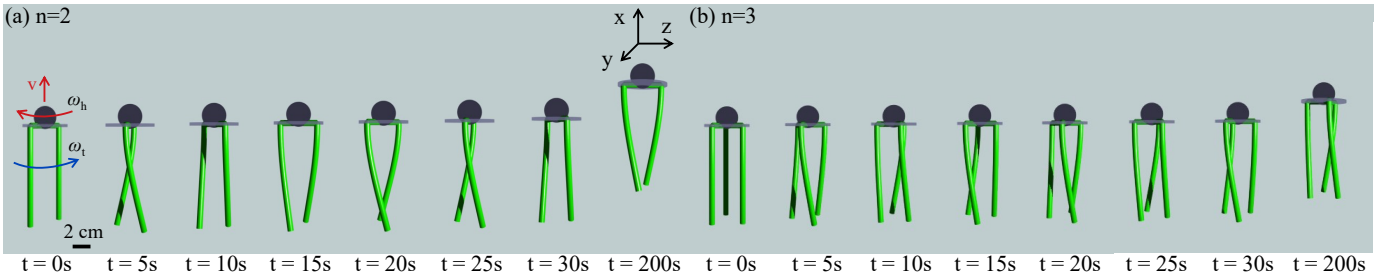

Fig. 1. Snapshots from simulation. The shape of a robot with (a) $n = 2$ tails (Rotational speed of the motor $\omega_T = 100.00$ rpm, head rotational speed $\omega_h = 95.47$ rpm, tail rotational speed $\omega_t = 4.53$ rpm) and (b) $n = 3$ tails ($\omega_T = 100.00$ rpm, $\omega_h = 97.49$ rpm, $\omega_t = 2.51$ rpm) between $t = 0$ and $t = 200$ seconds. The speed of the robot is $v = 0.22$ mm/s (and $v = 0.13$ mm/s) for $n = 2$ (and $n = 3$).

divided into two components: (1) external loading on the flexible structure from the surrounding medium and (2) articulated slender bodies composed of multiple thin elastic rods.

Model of external loading from GM: GM, such as sand, soil, muddy sediments, and other mechanically unstable terrestrial substrates, display solid-like behavior in bulk and fluid-like behavior when disturbed. A major challenge of modeling the nonlinear dynamics of soft robots in GM is modeling the external forces on thin filaments. Modeling the motion of soft robots in purely fluidic medium is possible by solving Navier-Stokes hydrodynamics in the presence of moving boundary conditions. However, the computational cost is prohibitive for application in design and control of soft robots. For rods – mechanical structures with one dimension much larger than the other two – moving in low Reynolds flow, RFT is widely used to connect the hydrodynamic force from viscous environment and the velocity along the rod's centerline [11], [18]. Despite differences in the physical mechanisms involved, a solid friction analog to RFT in viscous fluid has been successfully applied in the context of GM to describe the undulatory motion of sand lizards and snakes [19], [20]. Several studies have shown that the frictional forces perpendicular to the body per unit length are greater than those along the body [12], [21].

Mechanics of articulated elastic rod structures: As with bacteria, the head and tails of our untethered articulated robot rotate in opposite directions [13]. The external force induced by GM can result in geometrically nonlinear deformation of tails, as displayed in Fig. 1. Notable prior works investigated the force on thin *rigid* rods in viscous fluid [18] or GM [4], [5], [12]. Here, we use Discrete Elastic Rods (DER) [22]–[24] to capture the nonlinear deformation of thin elastic rods in the presence of external forces. The accuracy of DER has been established several times through prior works [25], [27], [36]. Previous studies combined DER with hydrodynamic models in viscous fluids to investigate the deformation and instability of a *single* helical elastic rod [25], [26]. Recently, we developed a model of multi-flagellated robots operating near the air-fluid interface [32].

A wide variety of soft robots can be modeled as a network of elastic rods, optionally connected to rigid bodies. Structures comprised of multiple elastic rods, e.g. elastic gridshell (also known as Cosserat net) [27] and flexible rod mesh [28], have also been modeled with DER. The multi-rod gridshell simulator [27] used stiff springs at the joints between two rods to impose constraints and computed the spring forces explicitly. This requires a smaller time step compared with an implicit approach and ignores the coupling of twisting and bending modes [28] between two rods at the joints. In this study, we present an algorithm that treats all the elastic and external forces implicitly in a network of rods and accounts for the presence of a rigid head. We demonstrate that a seemingly complex robot can be kinematically represented by a network of rods; this rod-based presentation can be used to leverage the computational efficiency of cutting edge tools like DER.

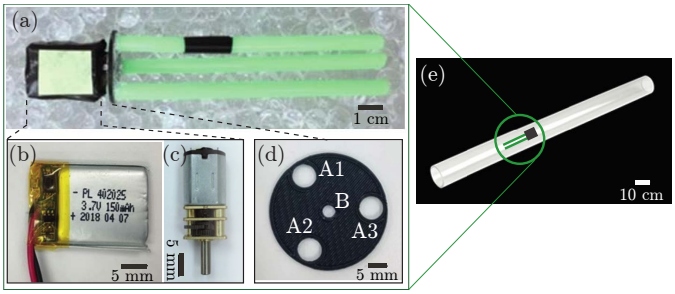

Fig. 2. The compositive view of the experimental setup. (a) The robot with $n = 3$ tails. The head is comprised of (b) a battery and (c) a motor. (d) A circular disc with a circular array of holes (holes A1-A3) for gluing the tails with Gorilla glue super glue, gel, and a centered hole (hole B) for inserting the motor shaft. (e) The robot is placed inside a cylindrical tube full of granular medium (transparent water beads in this work).

III. Experimental Design

Effective soft flagella-propelled locomotion in GM needs a complex interplay between the robot and GM, requiring back-and-forth iterations of robot design and GM selection. This section will detail the final robot design, GM, and the induced locomotion experiments.

A. Robot design

Fig. 2(a) shows a photograph of the soft robot which is a small, lightweight (14 cm, 35 g) structure actuated by n number of soft elastic tails that are made of Vinyl Polysiloxane (ZHERMACK Elite Double 32). It includes (1) a head with two 3.7V 200mAh rechargeable 502025 LiPo batteries (Fig. 2(b)) and one DC geared motor (uxcell) with 3V nominal voltage (Fig. 2(c)), 0.35W nominal power and 0.55A stall current, (2) multiple elastic tails, and (3) one 3D-printed plate ((Fig. 2(d))) to hold those tails. The elastic tails are fabricated straight using the molding and casting technique in [29]. The changeable inner and outer diameters of PVC tube molds make the scale-up or scale-down of our robot platform effortless. Inside the head, two batteries are connected in parallel, making

the entire structure symmetric. We design the robot head as cuboidal to increase its ability to fluidize the GM in front of it. The tails are inserted and glued (using Gorilla super glue, gel) into a circular array of holes on a 3D-printed plate and are driven by a motor via the shaft protruding from the robot head. We vary the number of tails to explore its effect on the translational speed, v, of our robot. The control parameter is the rotational speed of the tails relative to the head, ω_T. To modify it, we build robots with different motors but identical other components. The motor's rotational speed decreases as the voltage supplied drops. To ensure that the motor rotates at a constant speed, we fully charge the batteries before and after each 10-minute experiment. Moreover, the size and weight of all motors are almost the same, 13−15g and $(1.5-1.7)\times 1.2\times 1.0$ cm even though they provide different rotational speeds. When necessary, we wrap electrical tape around the motor to account for the minor differences in size and weight among different motors.

B. Granular medium & locomotion experiments

We choose water crystal beads as the GM to test the locomotion due to their transparency. The robot can be seen from outside the medium and its movement is recorded using a conventional digital camera (Nikon D3400) with a frame rate of 29.98fps. The diameter of the beads in dry state is 2.5 mm, which increases to $d_b = 9.4 \pm 0.4$ mm after fully absorbing water. The size of beads is determined by the amount of time they are placed inside water and reversible after dehydration. When performing experiments, we use the beads fully absorbing water to keep their size consistent. Before experiments are carried out, we dry their surfaces to decrease the possibility of slippage between the GM and the robot. The volume fraction [21] – the ratio between the solid volume and the occupied volume – is about 0.52. As illustrated in Fig. 2(a), the diameter of the beads is on the same order of magnitude as the diameter of the tails. RFT is intended for grains considerably smaller than the size of the robot; our choice of rather large grains is to test the limits of RFT.

As the reservoir for GM, we use a clear cylindrical tube with an inner radius of 5.3 cm and an axial length of 122 cm, as shown in Fig. 2(e). The tube is filled with GM and placed at a 2° angle to the horizontal plane to keep the GM compact while still allowing the robot to move. The robot is initially positioned at one end near the center of the cross-section of the tube, meant to cancel the wall effect. Since the robot is placed at the center of the tube, surrounded by compact granules against the tube wall, the drag-induced lift mentioned in [30] is suppressed. Hence, the rotation of tails propels the robot forward in a roughly straight line through the GM. A bright yellow marker is attached to the black colored head and a black marker is attached to one of the green colored elastic tails in order to count the rotational speed of the robot head (ω_h) and tail (ω_t).

IV. Numerical Model Description

Following experiments, we develop a simulator in Sections IV(A-E) to simulate the movement of the robot, with DDG simulating the structure by incorporating RFT for the drag force on the flagllum and Stokes's law for the force and torque on the robot head. The material and geometric parameters of the robot are given in Section IV(F).

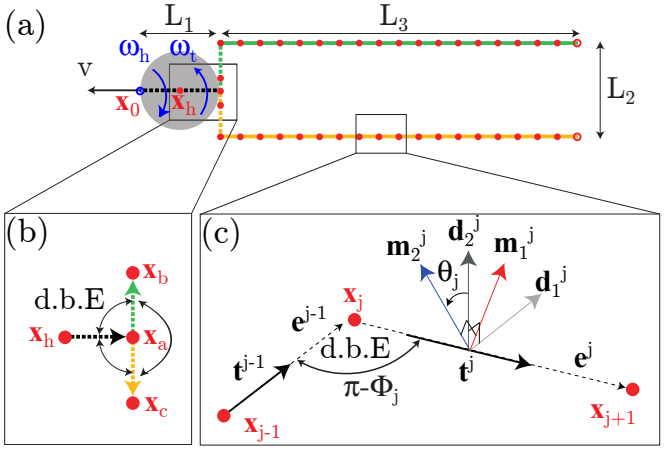

Fig. 3. Schematic of the discrete representation of a robot with $n = 2$ tails. (a) Geometric parameters of the robot in undeformed state. Here, $L_1 = 2a$ is the diameter of the robot head, L_2 is the diameter of the disc connecting the head and the tails, and L_3 is the length of each tail. Dashed lines represent rigid structure whereas solid lines correspond to flexible structure. Node $\mathbf{x}_h$ represents the location of the head. (b) A close-up of the "joint" node $\mathbf{x}_a$ that connects the head with tails. In this figure, d.b.E. indicates discrete bending and twisting energy between adjacent edges,i.e., $\mathbf{x}_h\mathbf{x}_a$, $\mathbf{x}_a\mathbf{x}_c$, and $\mathbf{x}_a\mathbf{x}_b$. This is the only node that is connected to more than two nodes. (c) A close-up of three nodes, $\mathbf{x}_{j-1}, \mathbf{x}_j$, and $\mathbf{x}_{j+1}$, and two edges, $\mathbf{e}^{j-1} = \mathbf{x}_j - \mathbf{x}_{j-1}$ and $\mathbf{e}^j = \mathbf{x}_{j+1} - \mathbf{x}_j$. The turning angle from edge $\mathbf{e}^{j-1}$ to $\mathbf{e}^j$ is ϕ_j. The reference frame on $\mathbf{e}^j$ is $\left\{\mathbf{d}_1^j, \mathbf{d}_2^j, \mathbf{t}^j\right\}$ and the material frame is $\left\{\mathbf{m}_1^j, \mathbf{m}_2^j, \mathbf{t}^j\right\}$. The twist angle on edge $\mathbf{e}^j$ is θ^j.

A. Kinematics

Referring to Fig. 3(a), the first step in modelling the robot is to represent it as a "stick figure". A number of nodes (circles in Fig. 3) are located along the stick figure. Fig. 3(b) shows the nodes at the "joint" between the head and tails ($n = 2$ in the figure). Node $\mathbf{x}_a$ is unique since it is connected to $n+1$ nodes. All other nodes are connected to two nodes or a single node in case of terminal nodes (open circles in Fig. 3(a)). As illustrated in Fig. 3(c), a node $\mathbf{x}_j$ is typically connected with two nodes $\mathbf{x}_{j-1}$ and $\mathbf{x}_{j+1}$. Details of concepts "edge" (e.g. $\mathbf{e}^j = \mathbf{x}_{j+1} - \mathbf{x}_j$), reference frame $\left\{\mathbf{d}_1^j, \mathbf{d}_2^j, \mathbf{t}^j\right\}$,and material frame $\left\{\mathbf{m}_1^j, \mathbf{m}_2^j, \mathbf{t}^j\right\}$ are given in our previous work [32]. Reference frame is initialized at time $t = 0$ and then updated at each time step of the simulation using time-parallel transport. Detailed DER can be found [22]–[24]. A scalar quantity, θ^j, is necessary per edge to obtain the material frame from the reference frame as outlined in Fig. 3(c). Angle θ^j is the "twist angle". We follow the convention of using subscripts to denote node-based quantities and superscripts for edge-based quantities.

The locations of the nodes, $\mathbf{x}_j$ ($0 \le j < N$ where N is the number of nodes), and the twist angles, θ^j ($0 \le j < N_e$ where N_e is the number of edges), completely describe the configuration of the robot. For the robot studied in this paper, $N_e = N - 1$ (see Fig. 3(a)). The DOF vector for the robot is $\mathbf{q} = \left[\mathbf{x}_0, \mathbf{x}_1, \mathbf{x}_2, \ldots, \mathbf{x}_{N-1}, \theta^0, \theta^1, \ldots, \theta^{N_e-1}\right]^T$, where the superscript ^{T} denotes transpose. If a robot has N nodes, the size of $\mathbf{q}$ is ndof $= 3N + N_e$. Since the robot deforms

with time, the DOF vector is a function of time, i.e. $\mathbf{q} \equiv \mathbf{q}(t)$. Knowing the configuration of the robot at $t = 0$ (i.e. $\mathbf{q}(0)$ is known), the task at hand is to compute $\mathbf{q}(t)$.

B. Macroscopic strains & Elastic energies

At time $t = 0$, the robot is undeformed with zero strains and the DOF vector is $\mathbf{q}(0) \equiv \bar{\mathbf{q}}$; hereafter, $\bar{(\,)}$ represents evaluation of a quantity in its undeformed configuration. Axial stretch, curvature, and twist are the macroscopic strains along the structure. The axial stretch, ϵ^j, in the j-th edge is

$$\epsilon^j = \frac{\|\mathbf{e}^j\|}{\|\bar{\mathbf{e}}^j\|} - 1. \tag{1}$$

Curvature binormal is a vector representing the turn whose proof is given in Fig. 3.2 and Eqs. 3.6 - 3.11 in [24]:

$$(\kappa\mathbf{b})_j = \frac{2\mathbf{e}^{j-1} \times \mathbf{e}^j}{\|\mathbf{e}^{j-1}\|\|\mathbf{e}^j\| + \mathbf{e}^{j-1} \cdot \mathbf{e}^j}. \tag{2}$$

It turns out that $\|(\kappa\mathbf{b})_j\| = 2\tan\left(\frac{\phi_j}{2}\right)$, where ϕ_j (in Fig. 3(c)) is the turning angle. No curvature is associated with the terminal nodes. The curvature of the osculating circle passing through $\mathbf{x}_{j-1}, \mathbf{x}_j$, and $\mathbf{x}_{j+1}$ is $\|(\kappa\mathbf{b})_j\|/\Delta l$ where $\Delta l = \|\mathbf{e}^j\| = \|\mathbf{e}^{j-1}\|$. The scalar curvatures along the first and second material directors are

$$\kappa_j^{(1)} = \frac{1}{2}(\mathbf{m}_2^{j-1} + \mathbf{m}_2^j) \cdot (\kappa\mathbf{b})_j, \tag{3a}$$

$$\kappa_j^{(2)} = \frac{1}{2}(\mathbf{m}_1^{j-1} + \mathbf{m}_1^j) \cdot (\kappa\mathbf{b})_j. \tag{3b}$$

Eqs. 3a and 3b and following equations were derived by [23] and a pedagogical exposition is available in [24]. In Fig. 3(c), the twist at the j-th node is

$$\tau_j = \theta^j - \theta^{j-1} + \Delta m_{j,\text{ref}}, \tag{4}$$

where $\Delta m_{j,\text{ref}}$ is the reference twist, i.e. the twist of the reference frame as it moves from the $(j-1)$-th edge to the j-th edge [22].

The total elastic energy of the structure is the linear sum of stretching E_s, bending E_b, and twisting E_t energies such that

$$E_{\text{elastic}} = E_s + E_b + E_t, \tag{5}$$

where E_s, E_b, and E_t are the quadratic functions of strains

$$E_s = \sum \frac{1}{2} EA \left(\epsilon^j\right)^2 \|\bar{\mathbf{e}}^j\|, \tag{6}$$

$$E_\text{b} = \sum \frac{1}{2}\frac{EI}{\Delta l_j}\left[\left(\kappa_j^{(1)} - \bar{\kappa}_j^{(1)}\right)^2 + \left(\kappa_j^{(2)} - \bar{\kappa}_j^{(2)}\right)^2\right], \tag{7}$$

$$E_t = \sum \frac{1}{2}\frac{GJ}{\Delta l_j}\left(\tau_j - \bar{\tau}_j\right)^2. \tag{8}$$

Here, $\sum$ in Eq. 6 represents summation over all the edges and curvatures in Eqs. 7 and 8. E is the Young's modulus, $A = \pi r_0^2$ is the cross-sectional area, and r_0 is the cross-sectional radius. $EI = \frac{\pi}{4}Er_0^4$ is the bending stiffness. G is the shear modulus and $GJ = \frac{\pi}{2}Gr_0^2$ is the twisting stiffness. For edges that are located on rigid parts (i.e. head and disc denoted by dashed lines in Fig. 3(a)), the stiffness parameters EA, EI and GJ are set sufficiently large to ensure negligible deformation. The Voronoi length $\Delta l_j = \frac{1}{2}\left(\|\bar{\mathbf{e}}^{j-1}\| + \|\bar{\mathbf{e}}^j\|\right)$ is associated with the j-th node. The material of tails is nearly incompressible (i.e. Poisson's ratio $\nu = 0.5$) and therefore $G = E/3$. Each internal node of a single elastic rod is associated with a discrete bending and twisting energy. However, a "joint" node ($\mathbf{x}_a$ in Fig. 3(b)) has multiple associated discrete bending (d.B.E. in Fig. 3(b)) and twisting energies. This observation is important during the implementation of the simulation algorithm.

C. External forces using Resistive Force Theory

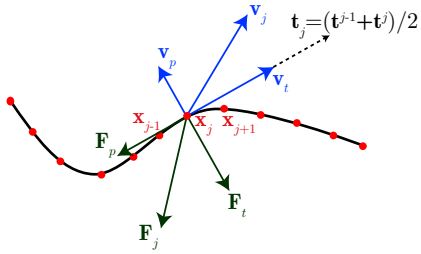

Fig. 4. Schematic representation of RFT.

In Fig. 4, we schematically represent a slender rod in the discrete setting moving in the GM. The velocity, $\mathbf{v}_j \equiv \dot{\mathbf{x}}_j$ at point $\mathbf{x}_j$ can be decomposed into two parts: the parallel term $\mathbf{v}_t = (\mathbf{v}_j \cdot \mathbf{t}_j)\mathbf{t}_j$ and the perpendicular term $\mathbf{v}_p = \mathbf{v}_j - \mathbf{v}_t$, where the tangent at the j-th node $\mathbf{t}_j = \frac{1}{2}(\mathbf{t}^{j-1} + \mathbf{t}^j)$ is the average of the tangents along the two associated edges. The external force on the flagellar j-th node is $\mathbf{F}_j = \mathbf{F}_t + \mathbf{F}_p$, where the tangential and perpendicular forces that resist $\mathbf{v}_t$ and $\mathbf{v}_p$ are

$$\mathbf{F}_t = -\eta_t \mathbf{v}_t \Delta l_j, \tag{9a}$$

$$\mathbf{F}_p = -\eta_p \mathbf{v}_p \Delta l_j, \tag{9b}$$

the drag coefficients along the tangential and perpendicular directions [11] are

$$\eta_t = 2\pi\mu \Big/ \left[\log\left(\frac{2L}{r_0}\right) - \frac{1}{2}\right], \tag{10a}$$

$$\eta_p = 4\pi\mu \Big/ \left[\log\left(\frac{2L}{r_0}\right) + \frac{1}{2}\right], \tag{10b}$$

μ is the constant used to quantify the body-granule friction coefficient, and L is the tail length($L = L_3$ in Fig. 3(a)).

The head rotates and translates as the robot moves. The rotational speed of the head (ω_h in Fig. 3) can be extracted from the time derivative of the twist angle, θ^h, of the edge connecting $\mathbf{x}_0$ and $\mathbf{x}_h$, i.e. $\omega_h \equiv \dot{\theta}^h$. The velocity of the head is $\mathbf{v}_h \equiv \dot{\mathbf{x}}_h$. If the head is spherical with radius a, the viscous drag on it according to Stokes's law is $\mathbf{F}_h = -6\pi\mu a\mathbf{v}_h$ and an external torque on the edge is $T_h = -8\pi\mu a^3\omega_h$. In our case, the robot head shape is not a sphere so we use numerical coefficients, C_1 and C_2, to account for the shape. As a result, the drag and torque are updated as follows

$$\mathbf{F}_h = -(6\pi C_1)\mu a\mathbf{v}_h, \tag{11}$$

$$T_h = -(8\pi C_2)\mu a^3\omega_h. \tag{12}$$

Overall, the GM is characterized by parameters C_1, C_2, and μ. If any of the physical properties of the medium, e.g., grain size, changes, these parameters will need to be updated.

D. Simulation loop, equations of motion

In the simulation scheme, time is discretized into small time steps (Δt) and the DOF vector, $\mathbf{q}$, is updated at each time step.

The equation of motion at the i-th DOF to march from $t = t_k$ to $t = t_{k+1} = t_k + \Delta t$ is

$$f_i \equiv \frac{m_i}{\Delta t}\left[\frac{q_i(t_{k+1}) - q_i(t_k)}{\Delta t} - \dot{q}_i(t_k)\right] + \frac{\partial E_{\text{elastic}}}{\partial q_i} - f_i^{\text{ext}} = 0, \tag{13}$$

where $i = 1, \ldots,$ ndof, the *old* DOF $q_i(t_k)$ and velocity $\dot{q}_i(t_k)$ are known, E_{elastic} is the elastic energy evaluated at $q_i(t_{k+1})$, f_i^{ext} is the external force (or moment for twist angles) on the i-th DOF, and m_i is the lumped mass at each DOF. Since the dynamics of the system is dominated by viscosity with negligible influence of inertia, the results presented in this paper do not vary with the mass parameters as long as low Reynolds number is maintained. Eq. 13 represents a system of ndof equations that has to be solved to obtain the *new* DOF $q_i(t_{k+1})$. Once the new DOF is obtained, the new velocity is simply $\dot{q}_i(t_{k+1}) = (q_i(t_{k+1}) - q_i(t_k))/\Delta t$.

Newton-Raphson method is used to solve the equations of motion. This involves solving the linear system $\mathbb{J}\Delta\mathbf{q} = \mathbf{f}$, where $\mathbf{f}$ is a vector of size ndof, the i-th component of this vector can be computed from Eq. 13, and $\mathbb{J}$ is a square Jacobian matrix for Eq. 13. The (i, j)-th component ($i, j = 1, \ldots,$ ndof) of the Jacobian is

$$\mathbb{J}_{ij} = \frac{\partial f_i}{\partial \xi_j} = \mathbb{J}_{ij}^{\text{inertia}} + \mathbb{J}_{ij}^{\text{elastic}} + \mathbb{J}_{ij}^{\text{ext}}, \tag{14}$$

where

$$\mathbb{J}_{ij}^{\text{inertia}} = \frac{m_i}{\Delta t^2}\delta_{ij}, \tag{15}$$

$$\mathbb{J}_{ij}^{\text{elastic}} = \frac{\partial^2 E_{\text{elastic}}}{\partial q_i \partial q_j}, \tag{16}$$

$$\mathbb{J}_{ij}^{\text{ext}} = -\frac{\partial f_i^{\text{ext}}}{\partial q_j}. \tag{17}$$

Here, δ_{ij} represents Kronecker delta. Evaluation of the gradient of the elastic energy ($\frac{\partial E_{\text{elastic}}}{\partial q_i}$) as well as its Hessian ($\frac{\partial^2 E_{\text{elastic}}}{\partial q_i \partial q_j}$) are well documented in [23], [24].

E. Main contributions & observations in the algorithm

An important contribution of this study is the observation that the actuation (e.g. rotation of motor) can be readily accounted for in the above framework by updating the undeformed configurations with time. Typically, undeformed configuration of a structure is fixed and assumed to be invariant through the simulation. The strains in undeformed configuration (e.g. $\bar{\kappa}_j^{(1)}, \bar{\kappa}_j^{(2)}, \bar{\tau}_j$) are used in calculation of elastic energies, their gradient (i.e. elastic forces), and Hessian. However, in case of this robot, the rotation of the motor causes the undeformed twist at the head node ($\mathbf{x}_h$) to vary with time. If the rotational speed of the motor is ω_T, we assume that the undeformed twist at the head node is $\bar{\tau}_h(t_k) = \omega_T t_k$. This results in rotations of the head (ω_h) and the tails (ω_t) along opposite directions such that $|\omega_T| = |\omega_h| + |\omega_t|$. The total rotational speed, ω_T, is a control parameter in this study.

The most computationally expensive part of the algorithm is solving the linear system. Observing and exploiting the sparsity of the Jacobian matrix, $\mathbb{J}$, is important to reduce computing time. Referring to Fig. 3(c), the entire structure is modelled as a series of stretching (e.g. one stretching spring is between $\mathbf{x}_j$ and $\mathbf{x}_{j+1}$) and bending-twisting springs (e.g. one bending-twisting spring is constructed by $\mathbf{x}_{j-1}, \mathbf{x}_j$, and $\mathbf{x}_{j+1}$). The stretching energy of each spring (Eq. 6) depends only on six DOFs (nodal coordinates of two nodes). For the stretching spring on edge $\mathbf{e}^j$, these DOFs are $\mathbf{x}_j$ and $\mathbf{x}_{j+1}$. The gradient vector $\left(\frac{\partial}{\partial \mathbf{q}}\left[\frac{1}{2}EA\left(\epsilon^j\right)^2\|\bar{\mathbf{e}}^j\|\right]\right)$ has only six non-zero terms and the Hessian matrix $\left(\frac{\partial^2}{\partial \mathbf{q}\partial \mathbf{q}}\left[\frac{1}{2}EA\left(\epsilon^j\right)^2\|\bar{\mathbf{e}}^j\|\right]\right)$ has only 6×6 non-zero terms. The bending and twisting energies of each spring (Eqs. 7 - 8) depend only on eleven DOFs, i.e. $\mathbf{x}_{j-1}, \theta^{j-1}, \mathbf{x}_j, \theta^j$, and $\mathbf{x}_{j+1}$ in case of the spring located at $\mathbf{x}_j$ in Fig. 3(c). The gradient vector and the Hessian matrix of these two energies therefore have only eleven and 11×11 non-zero terms. The full expressions for the gradient and Hessian terms are released [22], [24]; software implementation is also available [31][1]. The simulation requires the gradient of external forces (Eq. 17) expressed in Eqs. 9, 11, and 12. Their gradients with respect to the DOFs can be trivially obtained. Note that $\mathbb{J}_{ij}^{\text{ext}}$ is sparse. Since the expressions of all the Jacobian terms can be analytically evaluated and incorporated into the software, the simulation can use implicit method. In comparison with the explicit method, the implicit method typically can converge at larger Δt and requires less computation time. This is our second contribution.

Unlike the banded Jacobian in simulating a single elastic rod [23], the Jacobian here is only sparse but not banded due to the "joint" node. Another difference is the implementation of the gradient and Hessian of bending and twisting energies. As in Fig. 3, the gradient and Hessian in [23] assume that the tangent $\mathbf{t}^{j-1}$ points towards $\mathbf{x}_j$ and the second tangent $\mathbf{t}^j$ points forward from $\mathbf{x}_j$. The assumption does not always hold in this paper. For example, as represented in Fig. 3(b), we can have cases where both tangents (dashed arrows) point away from $\mathbf{x}_a$, the "joint" node. In this case, we can simply flip the first tangent ($\mathbf{t}^{\text{loc}} = -\mathbf{t}^{j-1}$) and use $\left\{\mathbf{d}_1^{\text{loc}} = -\mathbf{d}_1^{j-1}, \mathbf{d}_2^{\text{loc}} = \mathbf{d}_2^j, \mathbf{t}^{\text{loc}} = -\mathbf{t}^{j-1}\right\}$ as the "local" reference frame on edge $\mathbf{e}^{\text{loc}} = \mathbf{x}_j - \mathbf{x}_{j-1}$. The reference frame on the other edge $\mathbf{e}^j$ remains unchanged as $\left\{\mathbf{d}_1^j, \mathbf{d}_2^j, \mathbf{t}^j\right\}$. Flipping the edge also implies that the twist angle on $\mathbf{e}^{\text{loc}}$ in this local frame is $\theta^{\text{loc}} = -\theta^{j-1}$. This local representation in Fig. 3(b) can be used to compute the gradient and Hessian of the bending and twisting energies at $\mathbf{x}_j$ with respect to $\left\{\mathbf{x}_{j-1}, \theta^{\text{loc}}, \mathbf{x}_j, \theta^j, \mathbf{x}_{j+1}\right\}$ following the analytical expressions in [23]. Prior to including these gradient and Hessian terms in $\mathbf{f}$ (Eq. 13) and $\mathbb{J}$ (Eq. 14), we have to be mindful that $\frac{\partial}{\partial \theta^{j-1}}(\,) = -\frac{\partial}{\partial \theta^{\text{loc}}}(\,)$.

F. Physical parameters

The material and geometric parameters of the robot during experiments are: Young's modulus $E = 1.2 \times 10^6$ N/m^2, Poisson's ratio $\nu = 0.5$, density of the robot is 1000kg/m^3 (this is used to compute m_i in Eq. 13), and cross-sectional radius of tails $r_0 = 3.2$ mm. The length of each flagellum is $L_3 = 0.111$ m, radius of the robot head is $a = 0.02$ m, and the diameter of 3D-printed circular disc is $L_2 = 0.04$ m. Time step is $\Delta t = 10^{-2}$ s and the length of each edge on tails (in undeformed state) is $\|\bar{\mathbf{e}}^j\| = 4.11$ mm. We performed convergence studies to ensure that the size of temporal and

[1] https://github.com/QuantuMope/imc-der

spatial discretization ($\Delta t, \|\bar{\mathbf{e}}^j\|$) has negligible effect on the simulation results. The parameters μ, C_1, and C_2 will be fitted later in Section V-C.

V. Results and discussion

MATLAB reads images extracted from the recorded videos in Section III-B in sequence to track the positions of the robot, s, versus corresponding time points, t, and the speed of the robot $v = s/t$. The number of turns the head and tails of the robot rotate (N_h, N_t) are counted brute force, and used to calculate $\omega_h = N_h/t$, $\omega_t = N_t/t$. Recall from Fig. 1 that the motor embedded in the head generates a rotational speed, ω_T. The head and tails rotate in opposite directions with rotational speeds of ω_h and ω_t such that $\omega_T = \omega_h + \omega_t$ (ω_T, ω_h, and ω_t are all non-negative). The total rotational speed, ω_T, is considered as a control parameter in our study. The rotation of the tails generates an axial propulsive force (see Fig. 3). The entire system uses this propulsive force to move forward at a speed of v.

A. Threshold angular speed to move

Experiments reveal that there is a threshold below which the robot stays still ($v = 0$) and above which it starts to move. This is explicable in terms of granular mechanics. A threshold angular speed is necessary to convert the medium's behavior from solid to fluid. This threshold ω_T in our experiments is ≈ 50 rpm and thus there are no data points at $\omega_T \lesssim 50$ rpm. When $\omega_T \lesssim 50$ rpm, the tails and head still rotate relative to one another; however, the robot does not change its location. In this study, the maximum total angular speed is $\omega_T \approx 250$ rpm and the aforementioned regime ($\omega_T \approx 50$) is a relatively small part of the the overall parameter space. In simulations, we use RFT that does not consider this threshold. Nonetheless, the simulation can capture the motion of the robot when $v > 0$. It is straightforward to include this threshold in Section IV-D by imposing boundary conditions on the head. However, this will introduce new fitting parameters without significantly improving the overall predictive ability of the simulation.

B. Speed of the robot

During experiments, we used a digital camera to capture videos of the motion of the robot. Figs 5(a1) and (a2) show two snapshots of a robot with $n = 2$ tails and total rotational speed $\omega_T = 250$ rpm at $t = 0$ and $t = 300$ sec. The green tails were marked with black markers, and the black head was marked with a bright yellow marker. Aided by the transparency of the GM and the markers on the robot, these videos were processed to extract the position of the robot, s, as a function of time. Fig. 5(b) presents the position of the robot as a function of time. Closed triangles denote data from experiments, and the solid line represents a linear fit of the form $s = vt$. We observe that the robot moves at an almost constant velocity of $v \sim 0.6$ mm/s. This is expected from a solid body moving inside a medium governed by RFT.

Fig. 5(c) shows the position of a robot with $n = 4$ tails and rotational speed $\omega_T = 208$ rpm. The motion of the robot is now qualitatively different from the one presented in Fig. 5(b). The robot continuously moves forward in general but intermittently stays at the same position. This phenomenon is reminiscent of stick-slip – sudden motion that occurs when two multiple bodies are sliding past one another. At a larger number of tails (e.g., $n = 4$ and $n = 5$), experimental observations indicate that the GM can get jammed (i.e., increase in viscosity) and the robot frequently gets stuck. Interestingly, our experiments (see Fig. 5(b)) indicate the robot can resolve the jamming on its own through rotation (i.e., creating disturbance) for a few seconds. The periodic jamming or stick-slip cannot be captured by RFT and we do not include this behavior in our simulations. We focus only on robots with $n = 2$ and $n = 3$ tails that move at a constant speed with time. Nonetheless, this indicates room for expanding the theories for locomotion inside GM beyond RFT. Integrating such theories that describe the viscosity as a function of the robot configuration and time into the algorithm in Section IV-D should be relatively trivial.

C. Parameters fitting for simulations

Recall from Eqs. 11 and 12 that C_1 and C_2 are fitting parameters to account for the shape and surface roughness of the head. In addition, μ is the 3rd fitting parameter. As detailed next, experimental data with a 2-tailed robot ($n = 2$) are used to estimate C_1, C_2, and μ. Simulations are performed with these parameters for $n = 3$; simulation results are then compared against experiments for validation of the fitting process.

Figs. 6(a) and (b) present the speed of the robot, v, and the rotational speed of the head, ω_h, respectively, as functions of the total rotational speed, ω_T. The data for $n = 2$ and $n = 3$ are shown in the figures. The data (v vs. ω_T and ω_h vs. ω_T) for $n = 2$ are used to obtain the best fit values of the fitting parameters: $C_1 = 2.420, C_2 = 0.039$, and $\mu = 6.828$. These parameters are then used to simulate the locomotion of a robot with three tails. In Fig. 6(a), speed vs. total rotational speed data show good agreement between experiments and simulations. Fig. 6(b) shows the rotational speed of the head as a function of total rotational speed and we find that, in both experiments and simulations, a robot with $n = 3$ has a slightly larger head rotational speed than the one with $n = 2$.

The slight mismatch between the experimental and simulation data can be partially attributed to the assumptions made in the model. The fluid model assumes that the drag force exerted by the GM can be expressed using RFT. The structure model assumes that the tails are infinitesimally thin elastic rods. The drag force and torque on the head are assumed to be linearly proportional to its velocity and angular speed, respectively. Moreover, invariably there are experimental errors, e.g. structural defects introduced during fabrication. Nonetheless, the reasonably good agreement between experiments and simulations support the validity of RFT in this case.

D. Speed vs. number of tails

A counterintuitive discovery from Fig. 6(a) is that at a fixed value of the rotational speed of the motor, ω_T, the robot with 2 tails moves faster than the one with 3 tails. Additionally, the speed vs. total rotational speed curve is nonlinear. These observations point to the large structural deformation and strong coupling between the head and tails. As the number of tails, n, increases, the rotational speed of the head, ω_h, increases (at a fixed value of ω_T). Since $\omega_T = \omega_h + \omega_t$, this

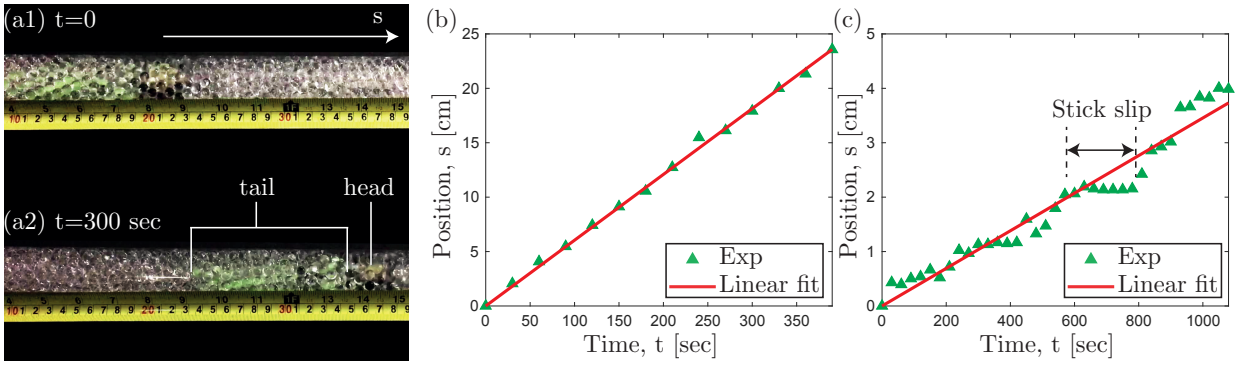

Fig. 5. Position of the robot with time. (a1-a2) Snapshots from experiments showing the location of a robot with $n = 2$ and $\omega_{\text{total}} = 250$ rpm at time $t = 0$ and $t = 300$ s. (b) Position, s, of the same robot as a function of time, t. Solid line corresponds to the linear fit $s = v\,t$ where v is the speed. (c) Position vs. time of a robot with $n = 4$ and $\omega_{\text{total}} = 208$ rpm, where stick-slip dynamics is prominent.

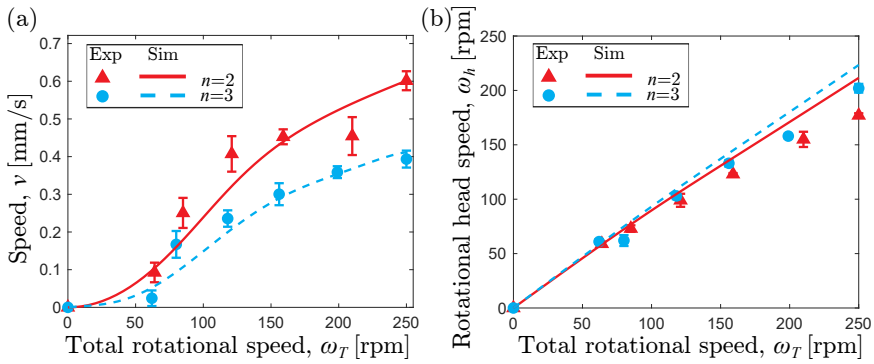

Fig. 6. Comparison between experiment data and simulation results for the relationship between(a) total rotation speed of head and tail and robot moving speed; (b)total rotation speed of head and tail and rotation speed of head. The red triangles and blue circles with error bars are experiment data when the tail number is 2 and 3 respectively. The solid red line is the simulated outcome associated with the fitting parameters, C_1, C_2, and μ whereas the dashed blue line represents the simulation result predicted by the same fitting parameters.

implies that the rotational speed of the tails, ω_t, decreases as n increases. The propulsive force generated by each tail (denoted as f_t) therefore also decreases. However, two additional factors to be considered to understand the overall speed, v, of the robot. First, the total propulsive force available is $n\,f_t$ and even though increasing n reduces f_t, it may (or may not) ultimately increase $n\,f_t$. Second, the total propulsive force is spent to overcome the drag on the head and the tail. As n increases, the amount of propulsive force spent on moving the tails forward also increases, and the propulsive force budgeted for the head decreases. All of these factors above combined dictate the dependence between the robot speed and the number of tails. Furthermore, our simulator predicts that for a small parameter space, an intersection exists between the relationship between the robot speed and the total rotational speed of the motor, such that the robot with more flagella can run faster than the robot with fewer flagella without experiencing "stick slip".

In the experiments presented herein, the set of physical parameters are chosen in such a way that the speed decreases with the number of tails. However, this is not universally true for this system. For example, consider a robot with $C_2 \to \infty$ in which the head never rotates (i.e. $\omega_h = 0$) and the rotational speed of the tail is always equal to the total rotational speed. Thus, f_t is a function of only ω_T (rather than n). Then, the total propulsive force, $n\,f_t$, increases with n (assuming ω_T is fixed) and the speed of the robot is also expected to increase.

E. Efficiency

The efficiency, η, of the robot is defined as the ratio of propulsive force to propulsive torque. Since η is a non-dimensional quantity, we choose the radius of the head, a, as the length scale. The expression for η is

$$\eta = \frac{|\mathbf{F}_h|}{|\mathbf{T}_h|}\,a = \frac{6\pi C_1 \mu a^2 v}{8\pi C_2 \mu a^3 \omega_h}, \tag{18}$$

where $|\cdot|$ denotes absolute value and expressions for $\mathbf{F}_h$ and $\mathbf{T}_h$ can be found in Eqs. 11 and 12, respectively. The numerator represents the drag force exerted on the robot by the medium, whilst the denominator gives the overall torque generated by the rotation of the motor. We use the simulator to predict the variation of efficiency, η, with the rotational speed, ω_T, as exhibited in Fig. 7. The efficiency of a robot with $n = 2$ is non-monotonic and peaks at $\omega_T \approx 150$ rpm. At this optimal rotational speed, the robot moves the farthest per unit motor torque. Such a clear presence of an optimal rotational speed in the operating range of the motor highlights the need of a numerical simulator that can be used to design robots. Moreover, for $\omega_T \lesssim 200$rpm, the efficiency of a two-tailed robot is greater than the one of a three-tailed robot. Beyond $\omega_T \gtrsim 200$rpm, the three-tailed robot outperforms the two-tailed robot. These findings underline the high degree of nonlinearity in the functional dependence between the efficiency and the physical parameters (e.g. n and ω_T).

VI. Conclusion

In this work, a discrete differential geometry(DDG)-based simulation framework was introduced where the robot is discretized into a number of mass-spring systems, with discrete elastic (bending, twisting, stretching) energies associated with each spring. The total elastic energy of the robot is the sum of all the discrete elastic energies. At each DOF, the sum of

elastic force (i.e. negative gradient of the elastic energy) and external force is equal to the lumped mass times acceleration of that DOF. The actuation of the robot (i.e. rotational speed of the motor) is represented by a time varying natural strain. This approach allows us to simulate the shape of the robot in a fully implicit manner.

We explore the physics of locomotion in GM with our simulation tool and an articulated robot testbed with multiple elastic tails. RFT – originally developed to model the hydrodynamics of low Reynolds fluid flow – was used to model the external force exerted by the GM. This force can be easily integrated into the simulation framework. Comparison between experiments and simulations showed that RFT is reasonably valid for flagellated robots discussed here. However, when the number of tails is large, "stick-slip" was observed and the underlying assumption behind RFT was no longer valid. Note that other types of external forces, such as gravity, hydrodynamics, and magnetic forces, can be easily incorporated to our simulation framework.

The simulation tool, supported by experiments, shed light on the highly nonlinear functional dependence between the performance of the robot (e.g. speed or efficiency) and the relevant physical parameters (e.g. number of tails). Some counter-intuitive observations include the inverse relation between the speed and number of tails of the robot. This happens when the robot is in a tube with different titled angles, e.g. 8°, 90°, the results of which are not displayed here because of the page limit. The non-monotonic dependence of efficiency on the rotational speed of the motor highlighted the necessity of a design tool for optimal control of the robot. The computational speed of the simulator can be exploited to run parametric studies and identify the optimal design and control of general articulated soft robots.

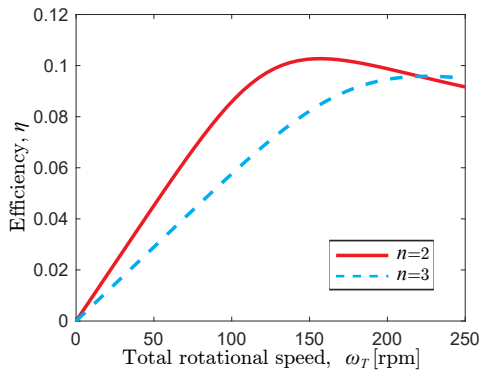

Fig. 7. Variation of torque utilization efficiency versus the total rotational speed of robot predicted by our simulator.

REFERENCES

[1] R. F. Shepherd, et al., "Multigait soft robot," *Proc. Natl. Acad. Sci.*, vol. 108, no. 51, pp. 20 400–20 403, 2011.

[2] M. T. Tolley, et al., "A resilient, untethered soft robot," *Soft Robot.*, vol. 1, no. 3, pp. 213–223, 2014.

[3] D. Rus and M. T. Tolley, "Design, fabrication and control of soft robots," *Nature*, vol. 521, no. 7553, p. 467, 2015.

[4] A. Thawani and M. S. Tirumkudulu, "Trajectory of a model bacterium," *J. Fluid Mech.*, vol. 835, pp. 252–270, 2018.

[5] H. Zhu et al., "A novel odor source localization system based on particle filtering and information entropy," *Rob. Auton. Syst.*, 132, pp. 103619, 2020

[6] F. Renda, et al., "A unified multi-soft-body dynamic model for underwater soft robots," *Int. J. Robot. Res.*, vol. 37, no. 6, pp. 648–666, 2018.

[7] A. A. Biewener, "Biomechanics of mammalian terrestrial locomotion," *Science*, vol. 250, no. 4984, pp. 1097–1103, 1990.

[8] M. H. Dickinson, et al., "How animals move: an integrative view," *Science*, vol. 288, no. 5463, pp. 100–106, 2000.

[9] G. K. Taylor, R. L. Nudds, and A. L. Thomas, "Flying and swimming animals cruise at a strouhal number tuned for high power efficiency," *Nature*, vol. 425, no. 6959, p. 707, 2003.

[10] T. Zhang and D. I. Goldman, "The effectiveness of resistive force theory in granular locomotion," *Phys. Fluids*, vol. 26, no. 10, p. 101308, 2014.

[11] J. Gray and G. Hancock, "The propulsion of sea-urchin spermatozoa," *J. Exp. Biol.*, vol. 32, no. 4, pp. 802–814, 1955.

[12] B. D. Texier, A. Ibarra, and F. Melo, "Helical locomotion in a granular medium," *Phys. Rev. Lett.*, vol. 119, no. 6, p. 068003, 2017.

[13] E. Lauga and T. R. Powers, "The hydrodynamics of swimming microorganisms," *Rep. Prog. Phys.*, vol. 72, no. 9, p. 096601, 2009.

[14] G. Olivier and D. Christian, "Fast, generic, and reliable control and simulation of soft robots using model order reduction,"*IEEE Trans. Robot.*, vol. 34, no. 6, p. 1565–1576, 2018.

[15] H. Jonathan and L. Hod, "Dynamic simulation of soft multimaterial 3d-printed objects,"*Soft Robot.*, vol. 1, no. 1, p. 88–101, 2014.

[16] K. Son, J. S. Guasto, and R. Stocker, "Bacteria can exploit a flagellar buckling instability to change direction," *Nat. Phys.*, vol. 9, no. 8, p. 494, 2013.

[17] G. Kirchhoff, "Uber das gleichgewicht und die bewegung eines unendlich dunnen elastischen stabes," *J. Reine Angew. Math.*, vol. 56, pp. 285–313, 1859.

[18] B. Rodenborn, et al., "Propulsion of microorganisms by a helical flagellum," *Proc. Natl. Acad. Sci.*, vol. 110, no. 5, pp. E338–E347, 2013.

[19] D. L. Hu, et al., "The mechanics of slithering locomotion," *Proc. Natl. Acad. Sci.*, vol. 106, no. 25, pp. 10 081–10 085, 2009.

[20] R. D. Maladen, et al., "Mechanical models of sandfish locomotion reveal principles of high performance subsurface sand-swimming," *J. R. Soc. Interface*, vol. 8, no. 62, pp. 1332–1345, 2011.

[21] R. D. Maladen, et al., "Undulatory swimming in sand: subsurface locomotion of the sandfish lizard," *Science*, vol. 325, no. 5938, pp. 314–318, 2009.

[22] M. Bergou, et al., "Discrete elastic rods," *ACM Trans. Graph*, vol. 27, no. 3, p. 63, 2008.

[23] M. Bergou, et al., "Discrete viscous threads," *ACM Trans. Graph*, vol. 29, no. 4, pp. 1–10, 2010.

[24] M. K. Jawed, A. Novelia, and O. M. O'Reilly, *A Primer on the Kinematics of Discrete Elastic Rods*. Springer, 2018.

[25] M. K. Jawed, et al., "Propulsion and instability of a flexible helical rod rotating in a viscous fluid," *Phys. Rev. Lett.*, vol. 115, no. 16, p. 168101, 2015.

[26] M. Jawed and P. M. Reis, "Dynamics of a flexible helical filament rotating in a viscous fluid near a rigid boundary," *Phys. Rev. Fluids*, vol. 2, no. 3, p. 034101, 2017.

[27] C. Baek, et al., "Form finding in elastic gridshells," *Proc. Natl. Acad. Sci.*, vol. 115, no. 1, pp. 75–80, 2018.

[28] J. Pérez, et al., "Design and fabrication of flexible rod meshes," *ACM Trans. Graph.*, vol. 34, no. 4, p. 138, 2015.

[29] J. Miller, et al., "Shapes of a suspended curly hair," *Phys. Rev. Lett.*, vol. 112, no. 6, p. 068103, 2014.

[30] R. D. Maladen, et al., "Undulatory swimming in sand: experimental and simulation studies of a robotic sandfish," *Int. J. Robot. Res.*, vol. 30, no. 7, pp. 793–805, 2011.

[31] A. Choi, et al., "Implicit contact model for discrete elastic rods in knot tying," *J. Appl. Mech.*, pp. 1–13, 2021.

[32] Y. Du, A. Miller and M. K. Jawed, " Simple flagellated soft robot for locomotion near air-fluid interface," *RoboSoft*, 2021

[33] F. Renda, et al., " Discrete Cosserat approach for soft robot dynamics: A new piece-wise constant strain model with torsion and shears," *Int. Conf. on Int. Rob. and Sys.*, pp. 5495-5502, 2016

[34] M. Hannan, and I. Walker, " Kinematics and the implementation of an elephant's trunk manipulator and other continuum style robots," *J. Robot. Syst.*, 20(2), pp. 45–63, 2003

[35] B. Jones, and I. Walker, "Kinematics for multisection continuum robots," *IEEE Trans. Robot.*, 22(1), pp. 43–55, 2006

[36] K. Jawed et al., "Coiling of elastic rods on rigid substrates," *Proc. Natl. Acad. Sci.*, 111(41), pp. 14663–14668, 2014